Nanoscale

PAPER

View Article Online
View Journal | View Issue

Cite this: *Nanoscale*, 2025, **17**, 3160

Percolative phase transition in few-layered $MoSe_2$ field-effect transistors using Co and Cr contacts†

Roshan Padhan, [a] Carlos Garcia,[b] Ralu Divan,[c] Anirudha V. Sumant, [c] Daniel Rosenmann, [c] Sujit A. Kadam, [a] Akshay Wali, [a,c] Suzanne Miller,[c] Stephen A. McGill *[b] and Nihar R. Pradhan *[a]

The metal-to-insulator phase transition (MIT) in two-dimensional (2D) materials under the influence of a gating electric field has revealed interesting electronic behavior and the need for a deeper fundamental understanding of electron transport processes, while attracting much interest in the development of next-generation electronic and optoelectronic devices. Although the mechanism of the MIT in 2D semiconductors is a topic under debate in condensed matter physics, our work demonstrates the tunable percolative phase transition in few-layered $MoSe_2$ field-effect transistors (FETs) using different metallic contact materials. Here, we attempted to understand the MIT through temperature-dependent electronic transport measurements by tuning the carrier density in a $MoSe_2$ channel under the influence of an applied gate voltage. In particular, we have examined this phenomenon using the conventional chromium (Cr) and ferromagnetic cobalt (Co) as two metal contacts. For both Cr and Co, our devices demonstrated n-type behavior with a room-temperature field-effect mobility of 16 $cm^2\ V^{-1}\ s^{-1}$ for the device with Cr-contacts and 92 $cm^2\ V^{-1}\ s^{-1}$ for the device with Co-contacts, respectively. With low temperature measurements at 50 K, the mobilities increased significantly to 65 $cm^2\ V^{-1}\ s^{-1}$ for the device with Cr and 394 $cm^2\ V^{-1}\ s^{-1}$ for the device with Co-contacts. By fitting our experimental data to the percolative phase transition theory, the temperature-dependent conductivity data show a transition from an insulating-to-metallic behavior at a bias of ~28 V for Cr-contacts and ~20 V for Co-contacts. This cross-over of the conductivity can be attributed to an increase in carrier density as a function of the gate bias in temperature-dependent transfer characteristics. By extracting the critical exponents, we find that the transport behavior in the device with Co-contacts aligns closely with the 2D percolation theory. In contrast, the devices with Cr-contacts deviate significantly from the 2D limit at low temperatures.

Received 28th September 2024,
Accepted 10th December 2024

DOI: 10.1039/d4nr03986f

rsc.li/nanoscale

I. Introduction

The rapid advancement of technology has intensified the demand for more efficient and high-performance devices.[1] With the growing use of smartphones, laptops, and data centers, there is an urgent need to address the increasing energy consumption and heat generation associated with these technologies.[2] There is an ongoing quest to explore quantum materials with tunable electronic properties for data storage and processing applications. Studying the metal-to-insulator transition (MIT) is particularly significant among various research avenues within two-dimensional (2D) systems.[3–6] MIT materials uniquely offer the ability to dynamically and reversibly switch between metallic and insulating states, reducing power consumption and significantly lowering heat generation.[3,6,7] This capability is crucial for the next generation of computing, communication, and storage technologies, as it enables faster and more reliable switching mechanisms while enhancing overall device efficiency.[3,8] Recent advancements in 2D transistors, such as sub-nm MoS_2 FETs, underscore the transformative potential of 2D materials in addressing scaling limitations and mitigating heat dissipation, further emphasizing the importance of studying MIT phenomena in these systems.[9] The theoretical foundation for understanding MITs in reduced dimensions was laid by the scaling theory of localization proposed by Abrahams *et al.*[10] which demonstrated that true metallic behavior is absent in two-dimensional disordered systems. Their work revealed how electronic conduc-

[a]*Layered Materials and Device Physics Laboratory, Department of Chemistry, Physics and Atmospheric Science, Jackson State University, Jackson, MS 39217, USA. E-mail: nihar.r.pradhan@jsums.edu*
[b]*National High Magnetic Field Laboratory, 1800 E. Paul Dirac Dr., Tallahassee, FL 32310, USA. E-mail: mcgill@magnet.fsu.edu*
[c]*Center for Nanoscale Materials, Argonne National Laboratory, 9700 S-Cass Avenue, Lemont, IL-60439, USA*

†Electronic supplementary information (ESI) available: Results of AFM, temperature scaling of conductivity, and percolation fitting for all temperatures. See DOI: https://doi.org/10.1039/d4nr03986f

tance transitions from logarithmic to exponential decay with increasing disorder or reduced system size, providing critical insights into transport phenomena at the nanoscale.

Among quantum materials, 2D transition-metal dichalcogenides (TMDCs) are ideal for studying the MIT due to their precise layer-dependent properties, high surface-to-volume ratio, and unique quantum confinement effects.[11–13] Their sensitivity to external stimuli allows for more controllable MIT behavior. At the same time, their flexibility and ease of integration into various device architectures enhance their utility in exploring and utilizing MIT phenomena.[12,13] Additionally, strong electron correlation effects in these materials make them particularly suited for examining the transition between metallic and insulating states. Among various 2D materials, $MoSe_2$ is particularly interesting due to its pronounced layer-dependent electronic properties, which shift from a direct to an indirect bandgap with changes in thickness.[14–16] Its high stability, tunable properties, and compatibility with other 2D materials make it an excellent candidate for studying the MIT.[13–15,17] Furthermore, $MoSe_2$ demonstrates superior FET device performance due to its high carrier mobility, excellent electrostatic control, and scalable fabrication, all of which enhance its ability to modulate current flow effectively in response to an applied electric field.[6,18–20]

This research extends our previous investigation of the MIT in few-layer $MoSe_2$ FETs at low temperatures, demonstrating tunable temperature scaling of the MIT, by using both traditional non-magnetic metallic and ferromagnetic contacts.[15] We explored the temperature-dependent transport properties of the 2D $MoSe_2$ devices using Cr and Co-contacts, which showed n-type behavior. The temperature-dependent conductivity data revealed an insulator-to-metal transition as a function of increasingcarrier density, analyzed through theoretical fits to the Fermi-liquid T^2-dependent relation. The temperature-dependent 4-terminal conductivities were analyzed using the temperature-dependent percolation theory and showed close agreement with a percolation-driven MIT throughout the studied temperature range for Co-contacts, while the Cr-contacted sample deviated from the predictions of the 2D percolation theory. The extracted critical exponents indicated that devices with Co-contacts closely followed the 2D percolation theory across the temperature range, whereas devices with Cr-contacts deviated from the 2D limit at low temperatures. The temperature-dependent data were also analyzed to understand the transport behavior through the Schottky barrier height (SBH). This work revealed the large difference in the SBH between Cr- and Co-contacted $MoSe_2$ devices that may also tune the MIT properties.

II. Results and discussion

$MoSe_2$ crystals were grown using the chemical vapor transport method and characterized before exploring their temperature-dependent transport properties.[15] Raman spectroscopy was employed to verify the quality of the crystals. Thin layers of flakes were mechanically exfoliated using blue tape and transferred onto a clean 285 nm thick SiO_2 layer deposited on a highly p-doped silicon substrate. The contacts were fabricated using Laser Writer-based optical lithographic techniques, followed by e-beam evaporation (Lesker PVD 250 at a base pressure of 10^{-8} Torr) of Au (80 nm)/Cr (5 nm) for Au/Cr contacts and Au (80 nm)/Co (10 nm) for Au/Co-contacts. Several devices were also fabricated using a Temescal e-beam evaporator in a clean room environment. The thickness of the $MoSe_2$ layer was 7–15 nm as measured by atomic force microscopy. Fig. 1(a) shows the optical micrograph image of the 7 nm thick $MoSe_2$ FET devices with contacts of 5 nm Cr and 80 nm Au. Fig. 1(b) shows a 7 nm thick $MoSe_2$ device with 10 nm Co and 80 nm Au fabricated on a 285 nm SiO_2 substrate deposited on highly p-doped Si. The thicknesses of the devices were measured using a Veeco Dimension Atomic Force Microscope (AFM). The AFM topography and height measurements are shown in the ESI Fig. S1.† The devices were covered with a thin layer of Cytop polymer to protect them from direct contact with the ambient atmosphere. The transport measurements shown in Fig. 1 were carried out using the 2-terminal method and all temperature dependent transport measurements were performed using the 4-terminal method shown in Fig. 2–5 to eliminate the associated resistance of the contacts. We measured the drain-source current (I_{ds}) as a function of the drain-source voltage (V_{ds}) using two terminals as shown in Fig. 1(c and d) for Cr-contact $MoSe_2$ (Cr-$MoSe_2$) and Co-contact $MoSe_2$ (C-$MoSe_2$) FETs at different applied gate voltages (V_{bg}). We observed the linear *I–V* curve on both Cr- and Co-contacted devices although they were Schottky contacts due to the thermionic emission process at room temperature. Fig. 1(e and f) shows the transistor characteristic I_{ds} as a function of applied gate voltage V_{bg} for Cr-$MoSe_2$ and Co-$MoSe_2$ respectively.

The drain current appears higher in the Co-$MoSe_2$ device compared to the Cr-$MoSe_2$ device for devices with the same thickness of $MoSe_2$, which indicates that the Co-contact could be better than the Cr-contact on $MoSe_2$. The extracted field effect mobilities using the Si-MOSFET formula for 2-terminal devices, $\mu_{FE} = \frac{L}{WC_{ox}V_{ds}} \times \left(\frac{dI_{ds}}{dV_{bg}}\right)$, yields mobility values of 6.5 $cm^2\ V^{-1}\ s^{-1}$ and 15.2 $cm^2\ V^{-1}\ s^{-1}$ for Cr-$MoSe_2$ and Co-$MoSe_2$ respectively. The parameter L is the channel length between two current contacts where V_{ds} was applied and current was measured on the same outer (current) contacts. C_{ox} = 11 : 505 × 10^{-9} F cm^{-2} is the capacitance/unit area between the gate and the channel for a 285 nm layer of SiO_2. $C_{ox} = \varepsilon_o\varepsilon_r/d$, ε_r = 3.9 for SiO_2 and d = 300 nm. We also measured the four-terminal transport measurements for these devices shown in the ESI Fig. S2.† Fig. S2(a and b)† present the I_{ds} *vs.* V_{bg} values of the Cr-$MoSe_2$ and CoMoSe_2 devices. The four-terminal mobility values are extracted using the MOSFET relation $\mu_{FE} = \frac{l}{WC_{ox}}\left(\frac{d(I_{ds} - I_0)/V_{12}}{dV_{bg}}\right)$, where l is the channel length of the devices between two voltage contacts (inner contacts in 4-terminal measurements), which was

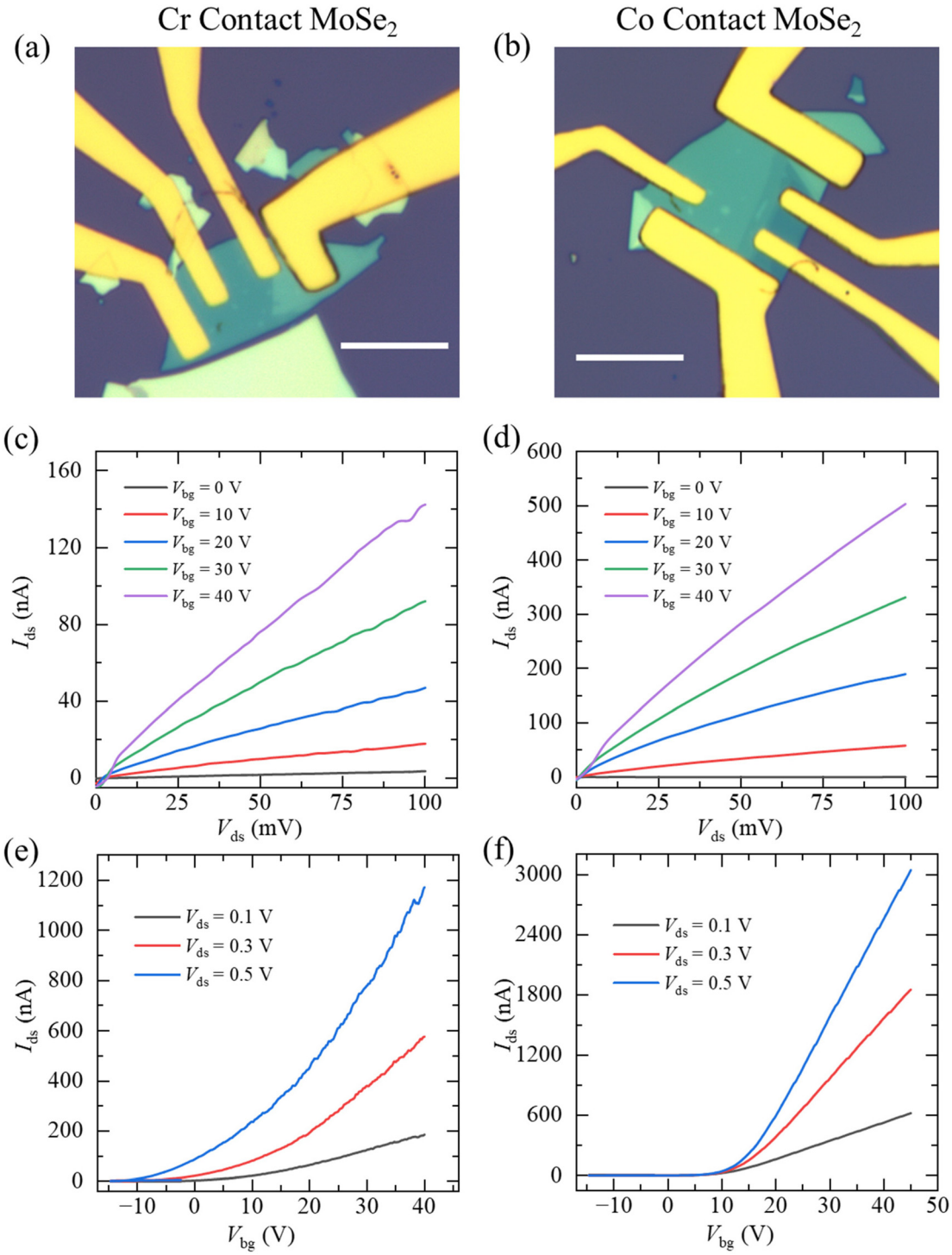

Fig. 1 Room temperature FET characterization: (a and b) optical micrograph of $MoSe_2$ devices with Co/Au contact and Cr/Au contact (scale bar: 10 μm), (c and d) basic output characteristics of FET at different back-gate voltages (V_{bg}) for both Co- and Cr-contact $MoSe_2$ FETs measured at room temperature, (e and f) transfer characteristics of FETs at different source-drain voltages (V_{ds}).

9.5 μm for the Cr-contact device and 8 μm for the Co-contact device. W is the width of the channel of the devices and the values are 5.4 μm for Cr and 4.78 μm for Co-contacts. C_{ox} is the gate capacitance as stated before and I_0 is the current in the subthreshold regime. V_{12} is the voltage sense between two voltage contacts (inner contacts) in 4-terminal measurements. The value of $\left(\frac{d(I_{ds}-I_0)/V_{12}}{dV_{bg}}\right)$ was extracted from the slope of the I_{ds} curve in the linear region. In both cases, μ_{FE} increased with decreasing temperature.[6,21–25] We found that the field

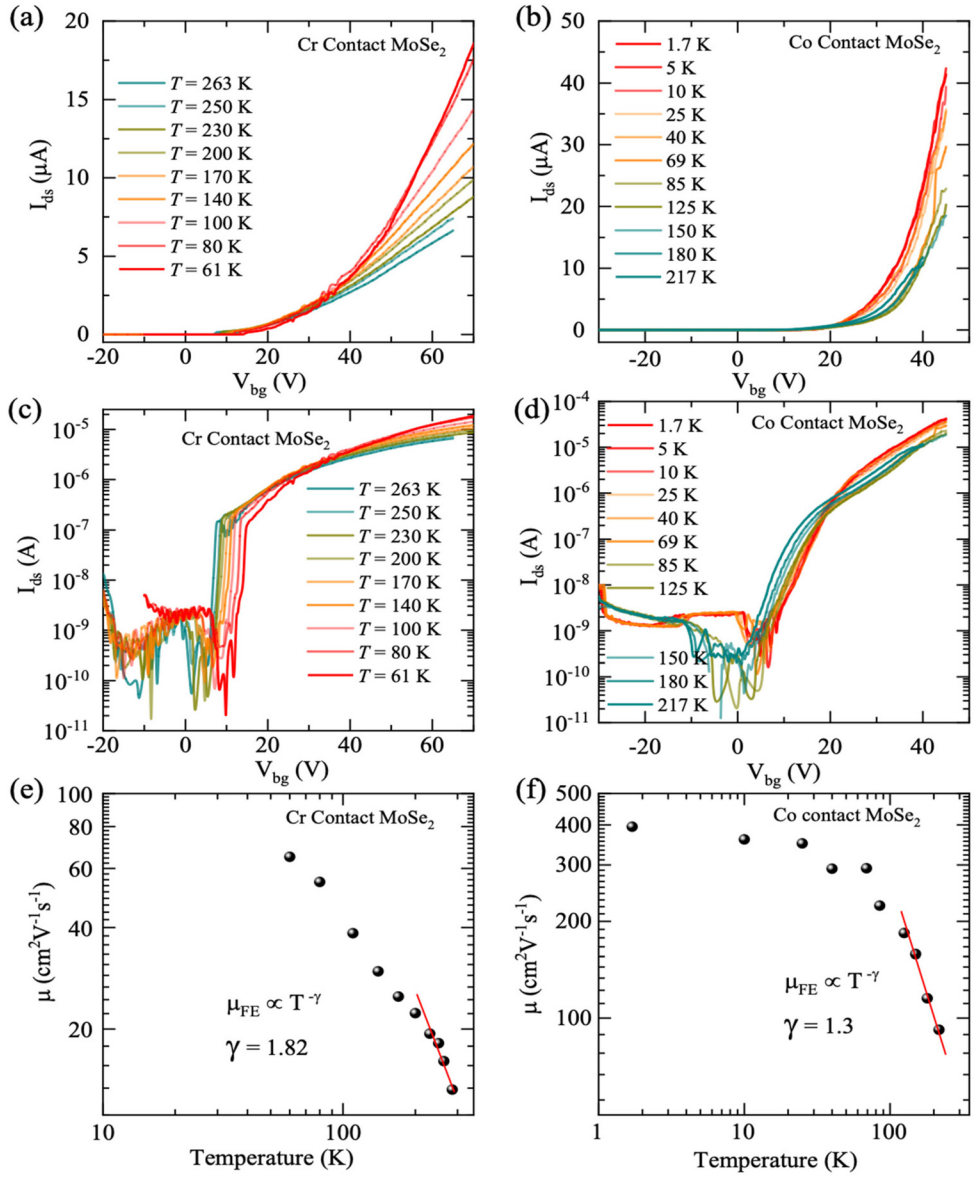

Fig. 2 Temperature dependent electrical transport measurement: (a) and (b) transfer characteristics of $MoSe_2$ FET at different temperatures for Cr-contacts and Co-contacts, respectively, measured at V_{ds} = 500 mV, (c) and (d) transfer characteristics of $MoSe_2$ FET at different temperatures for Cr-contacts and Co-contacts in the semi-logarithmic scale, (e) and (f) display the temperature dependent field-effect mobility of the $MoSe_2$ devices for Cr- and Co-contacts, respectively. (The red line indicates the power law fitting for phonon-limited mobility.)

effect mobilities at room temperature of these devices increased to 16 $cm^2\ V^{-1}\ s^{-1}$ and 45.5 $cm^2\ V^{-1}\ s^{-1}$ for Cr-$MoSe_2$ and Co-$MoSe_2$ FETs in 4-terminal measurements.

Fig. S2(c and d)† show comparison plots of 2- and 4-terminal measurements of transport curves from where we extracted the contact resistance of the device using the relation $R_c = \frac{1}{2}\left(\frac{V_{ds}}{I_{2T}} - \frac{V_{ds}}{I_{4T}}\right)$, where I_{2T} and I_{4T} are the drain currents measured from the 2- and 4-terminal configurations respectively. The contact resistances shown in Fig. S2(e and f)† suggest a higher value in the Cr-$MoSe_2$ FET compared to that in the Co-$MoSe_2$ FET. The R_c values for the Cr-$MoSe_2$ and Co-$MoSe_2$ devices are 3 MΩ, 2.7 MΩ (at V_g = 15 V), 1.6 MΩ, 1.2 MΩ (at V_g = 20 V) and 600 KΩ, 200 KΩ (at V_g = 35 V). This could explain why the Co-$MoSe_2$ device performs better than the Cr-$MoSe_2$ FET. Our aim was to explore the temperature-dependent transport behavior of the FETs based on these two different metal contacts and how the conductivities could be tuned as a function of applied gate voltage (*i.e.*, charge carrier density). The conductivities revealed the intrinsic behavior of the $MoSe_2$ when analyzed with temperature-dependent scaling. We measured another set of devices for a temperature dependent study as described below. Fig. 2(a) and (b) display the four-terminal drain-source current, I_{ds}, as a function of

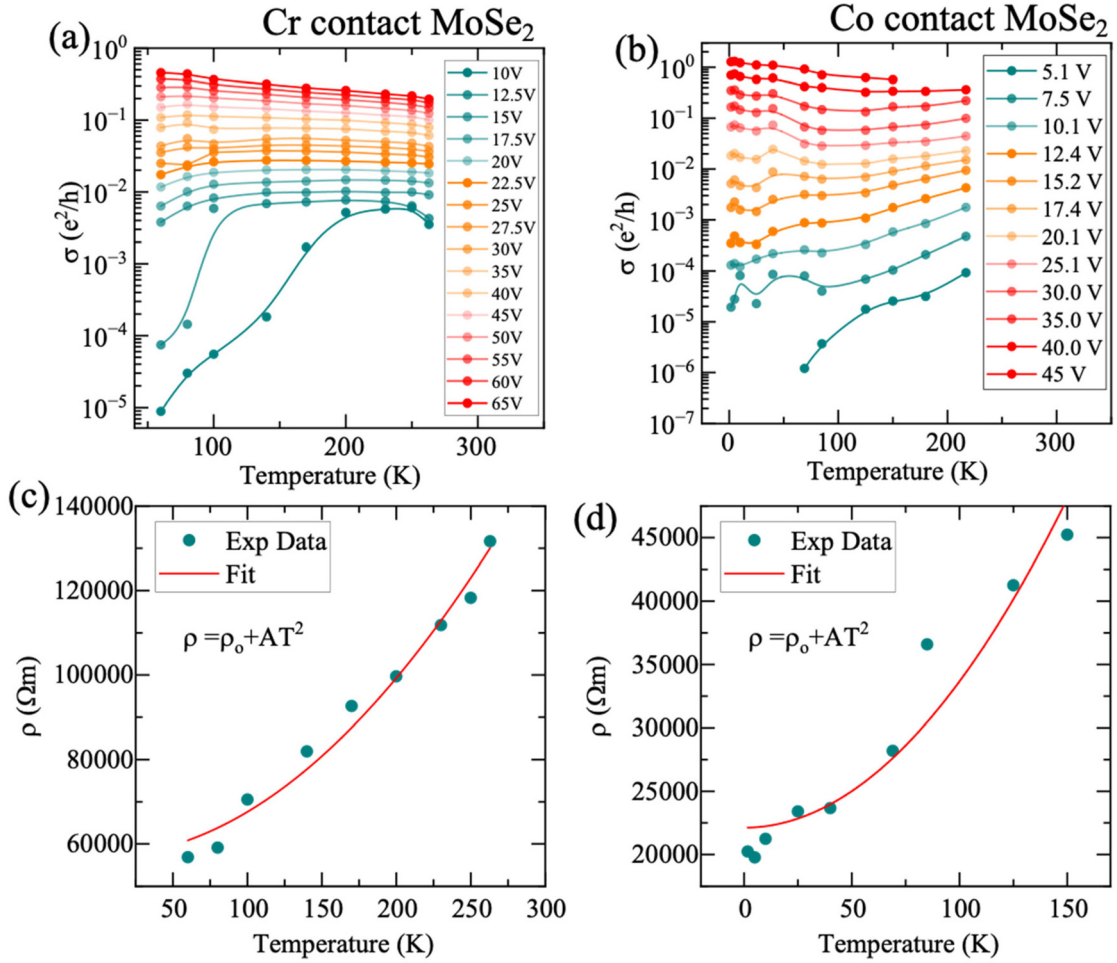

Fig. 3 Temperature-dependent conductivity variations: (a and b) *T*-dependent conductivity at different back-gate voltages for Cr-contacts and Co-contacts, (c and d) Fermi-liquid model fitting of resistivity at a back-gate voltage of 20 V, for Cr-contacts and Co-contacts.

back gate voltage, V_{bg}, at several different temperatures under a constant drain-source voltage of V_{ds} = 500 mV for the devices with Cr- and Co-contacts, respectively. The device showed n-type FET behavior, similar to earlier reports on $MoSe_2$-based FET devices.[15,26] The threshold voltage was ~20 V for both devices, and at V_{bg} = 0 V, a charge carrier density of $n \approx 1.59 \times 10^{12}$ cm^{-2} was induced in the $MoSe_2$ channel. The semi-logarithmic scaled I_{ds} values as a function of V_{bg} are shown in Fig. 2 (c and d) for both Cr- and Co-contacted devices. The observed ON/OFF current ratio of ~10^5 showed the comparable performance of the previously reported multilayered TMDC-based devices.[15,23,27,28] Fig. 2(e and f) display the extracted field-effect mobilities as a function of temperature for Cr- and Co-contacted devices. The field-effect mobilities were extracted from the semiconducting MOSFET relation as explained before where l is the channel length of the devices between two voltage contacts (9.5 μm for the Cr-contact device and 8 μm for the Co-contact devices) and W is the width of the fabricated devices (5.4 μm for Cr and 4.78 μm for Co-contact devices). As shown in Fig. 2(e), for the Cr-contacted device, μ_{FE} was determined to be 16 cm^2 V^{-1} s^{-1} at 263 K and 65 cm^2 V^{-1} s^{-1} when cooled to 61 K. In contrast, the field-effect mobility for the Co-contacted FET (Fig. 2(f)) was 92 cm^2 V^{-1} s^{-1} at 217 K and increased to 394.8 cm^2 V^{-1} s^{-1} when cooled to 1.7 K. Such a difference in mobility for the Co-contacted $MoSe_2$ device demonstrates the significance of using a suitable contact with a high charge injection capacity. Furthermore, cobalt is ferromagnetic, and spin current injection could be another factor that could potentially lead to a reduction in scattering mechanisms through spin–orbit coupling, thereby indirectly enhancing mobility by mitigating certain types of electron scattering events in the Co-$MoSe_2$ device. The mobility obtained is considerably higher than those previously reported for $MoSe_2$-based field-effect transistors with traditional metal contacts.[29–31] Furthermore, for both types of contacts, these devices showed strongly *T*-dependent mobilities, indicating phonon and impurity scattering. At lower temperatures, the phonon scattering of the sample was minimized, resulting in electron mobility being limited by the scattering by impurities and crystal defects. In general, electron–phonon (e–ph) scattering plays a key role in carrier mobility near room temperature.[32,33] Longitudinal optical (LO) phonon scattering

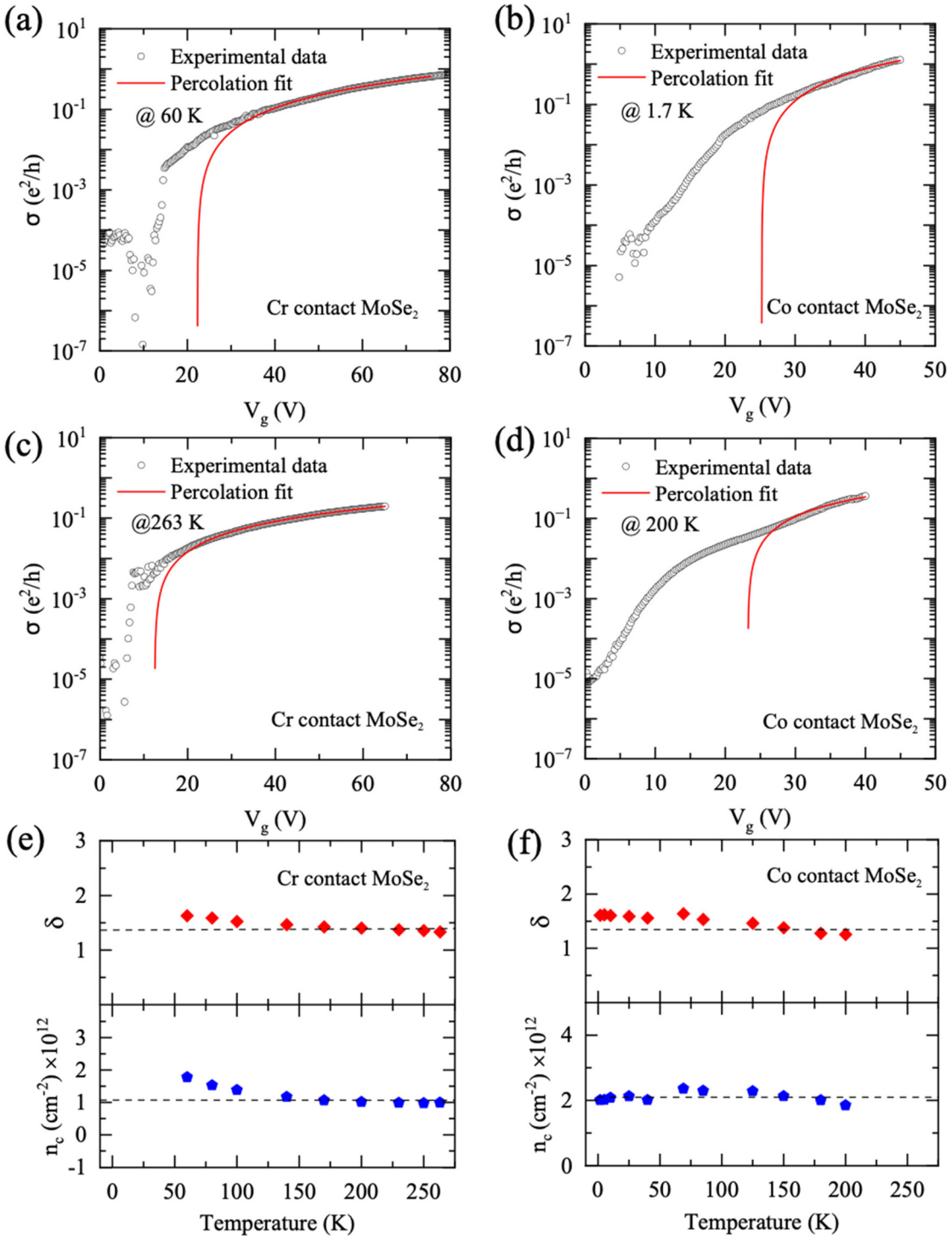

Fig. 4 Percolation type phase transition model: the percolation fitting of the conductivity variation data with respect to back-gate voltage at various temperatures (a and c) for Cr-contacted and (b and d) for Co-contacted $MoSe_2$ devices. (e and f) The extracted values of the critical exponent and critical carrier density for Cr-contacts and Co-contacts in the above fitting at different temperatures.

limits the intrinsic mobility of most transition metal dichalcogenides, while for MoS_2 and WS_2, the mobility is limited by longitudinal acoustic (LA) phonon scattering.[32]

Following the phonon scattering theory, we fitted the T-dependent mobility to the power law, *i.e.*, $\mu_{FE} \propto T^{-\gamma}$, where γ = the phonon scattering exponent. The γ value for the Cr-contacted $MoSe_2$ FET was 1.82, whereas it was 1.3 for the Co-contacted $MoSe_2$ FET. The smaller γ for the Co-contacted $MoSe_2$ FET is associated with a comparatively lower phonon scattering than in the Cr-contacted device. Below 70 K, the phonon

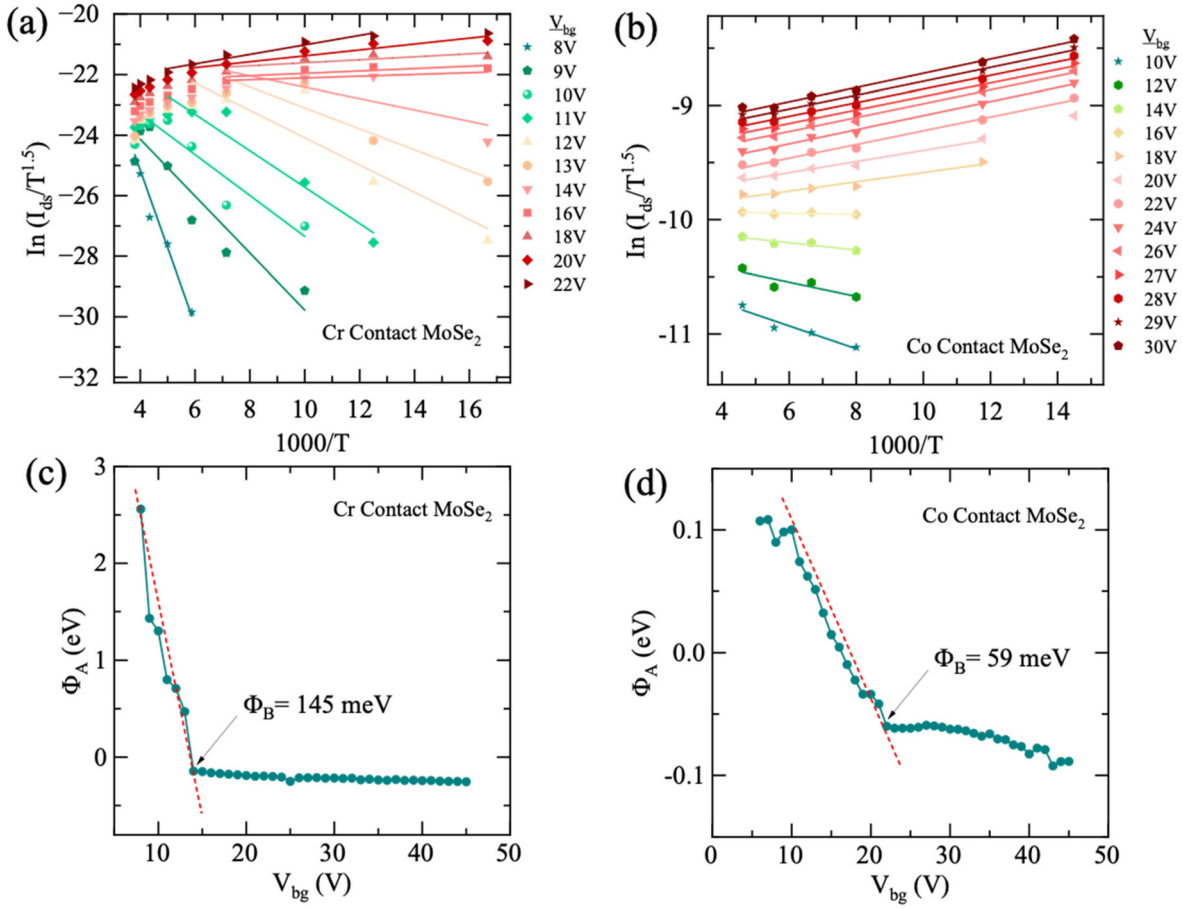

Fig. 5 Schottky barrier height calculation: (a and b) Arrhenius plot for Cr-contacts and Co-contacts at different back-gate voltages, (c and d) activation energy as a function of the back-gate voltage for both contact types (Schottky barrier height was extracted from the curve).

scattering is minimized; however, scattering due to impurity and defects states, carrier localization, and the Schottky barrier leads to saturation in the T-dependent mobility. The Co-contacted device showed the highest mobility, ~400 cm^2 V^{-1} s^{-1} between 10 and 2 K. Similar T-dependent mobility was reported on $MoSe_2$ FETs fabricated on a SiO_2/Si substrate.[15]

Fig. 3 displays a deeper analysis of the temperature-dependent conductivities of the Cr- and Co-contacted $MoSe_2$ devices. The quantized conductivity (σ) was calculated from the temperature dependent I_{ds} *vs.* V_{bg} graph using the relation $\sigma = \frac{WI_{ds}}{lV_{ds}} \times \frac{e^2}{h}$, where e is the charge of the electron and h is Planck's constant. The 4-terminal conductivity as a function of temperature at several applied back gate voltages is depicted in Fig. 3(a) for the Cr-contacted $MoSe_2$ FET. This device showed typically semiconducting behavior below V_g = 27.5 V, *i.e.*, σ decreased with decreasing temperature. Conversely, above an applied gate voltage of 27.5 V, the device showed metallic behavior, *i.e.*, σ increased with decreasing temperature. This indicates that upon injecting a high carrier density, the metallic phase emerged from the insulating phase at low temperatures. We also performed a similar T-dependent conductivity analysis for the Co-contacted device at different gate voltages (5.1–45 V) as depicted in Fig. 3(b). In this case, the transition from metallic to insulating behavior was observed at a comparatively lower back gate voltage of 20.1 V. To elucidate the nature of the phase transition, we renormalized the T-dependent conductivity plot with critical conductivity (σ_c), acquired from the transition point (V_{bg} = 27.5 V for Cr-contacts and V_{bg} = 20.1 V for Co-contacts) as shown in the ESI† and then scaled it with the temperature parameter T_o (ESI Fig. S3†). However, the temperature scaling failed similarly to the previously reported Cr-contact.[15] However, our temperature dependent scaling of the conductivity and critical exponent more closely matched the percolation type of phase transition as discussed below. According to the Fermi-liquid model of conductors, resistivity ($\rho = \sigma^{-1}$) is related to temperature through the relation $\rho = \rho_0 + AT^2$, where ρ_0 is the resistivity at 0 K. To verify the metallic behavior at higher gate voltages, we evaluated the resistivity of the channel as a function of temperature. Fig. 3(c) shows the resistivity of Cr-contacted $MoSe_2$ at an applied back gate voltage V_{bg} = 45 V, and Fig. 3(d) shows the resistivity of the Co-contacted device at V_{bg} = 65 V. In both cases, the data fit the Fermi-liquid equation well, as indicated by the red line of the

plot. A similar metallic conductivity was observed in ReS_2 where the resistivity was fitted with the Fermi-liquid T^2 dependent equation throughout the temperature range at higher carrier densities or applied gate voltages.[34] This theoretical fitting shows the hallmark of metallic behavior of the $MoSe_2$ FET.

We analyzed the temperature-dependent conductivities with the percolation model, and the data are shown in Fig. 4. The temperature-scaled percolation model formulates the relation between conductivity (σ) and the carrier density (n) as $\sigma = A(n - n_c)^{\delta}$, where n_c is the critical carrier density beyond which the carriers can form a percolating path in the random network of charged carriers between the source and the drain.[22,35] From the theoretical predictions, $\delta = 1.33$ for 2D percolation.[15,19,22,36] The density of charge carriers induced at the interface can be controlled by applying the back gate voltage. The induced carriers can be obtained from the relation $n = C_{ox} \times V_{bg}/e$; hence the percolation prediction for conductivity can be written in terms of V_{bg} as $\sigma = (A \times C_{ox}/e)(V_{bg} - V_c)^{\delta}$, where V_c is the critical back gate voltage. We fitted all the temperature-dependent curves with the percolation fits, and two of those fits are shown in Fig. 4(a and c) for the Cr-contacted $MoSe_2$ device. Similarly, the percolation fits for the Co-contacted $MoSe_2$ device are shown in Fig. 4(b and d). More temperature dependent percolation fits are shown in the ESI Fig. S4 and S5.† We extracted the critical exponents δ and V_c from which the critical carrier density n_c was calculated. The δ and n_c values were plotted as a function of temperature and are shown in Fig. 4(e) and (f), respectively, for Cr- and Co-contacted $MoSe_2$ devices. For the Cr-contacts, the critical exponent lies almost between 1.33 and 1.4, which is the theoretical predicted value of a 2D percolation phase transition, $\delta = 1.33$. The δ value deviated from the theoretical prediction when the device was cooled below 100 K reaching 1.63 at 61 K. For Cr-contacts, the critical carrier density (n_c) showed a slight increase with decreasing temperature while the Co-contacted device showed almost temperature independent carrier density. Due to the low contact resistance (R_c) in the Co-contact device, the current (or conductivity) values showed saturation at such applied gate voltages compared to the high contact resistance in the Cr-contacted device as we decreased the temperature. The I_{ds} *vs.* V_g data in Fig. 2(a–d) show that the conductivity values in the Co-contacted device were nearly four times higher than those in the Cr-contacted device. Thus, the carrier density was still increasing with temperature in the Cr-contact compared to the Co-contact device. This behavior suggests that Co-contacts provide a more efficient carrier injection mechanism, even at low temperatures, leading to constant n_c values. These differences reflect the distinct interaction of Cr and Co with $MoSe_2$, likely arising from variations in their work functions, interface chemistry, and surface roughness. Previously, Pradhan *et al.*[15] reported that the value becomes ~2 at 5 K.[2] However, by changing this contact to Co, we have achieved a consistent value near the theoretical predicted value even at low temperatures down to 1.7 K. The constant term, A, depends upon factors like contact resistance (R_c), surface roughness, and the measurement method (*i.e.*, 4-wire/2-wire measurement). Hence, we also found different values of A in the fabricated $MoSe_2$ devices by changing the type of contact. From percolation fitting, the value of A was found to be 0.01 for the Cr-contacts and 0.001 for the Co-contacts.

The obtained critical carrier densities for both Cr- and Co-contacted $MoSe_2$ as a function of temperature are displayed in Fig. 4(e) and (f). For Cr-contacts we obtained the average critical carrier density $n_c \approx 1 \times 10^{12}$ cm^{-2} (dashed line in Fig. 4e). In contrast, a higher n_c of $\sim 2 \times 10^{12}$ cm^{-2} was achieved in the Co-contacted $MoSe_2$ FET.

So far, from the above discussion of our conductivity analysis, the Co-contacted $MoSe_2$ device showed a stable 2D percolative phase transition and much higher charge carrier mobility than the Cr-contacted device. To further examine the stability of the Co/$MoSe_2$ interface and analyze the carrier injection from metal to semiconductor, we extracted the Schottky barrier height (SBH) for both types of contacts. The SBH was extracted from the temperature-dependent transfer characteristics of a 2D FET using the following Arrhenius equation for thermionic emission in a 2D system:[6,27,37,38]

$$\ln(I_{ds}/T^{3/2}) = \ln A + \ln A_{2d} - \frac{\Phi_A}{K_B}\left(\frac{1}{T}\right)$$

where A_{2d} is Richardson's constant in a 2D system, A is the area of the contact, K_B is the Boltzmann constant, and Φ_A is the activation energy. This equation is the linear form of the well-known Arrhenius plot. The slope of the Arrhenius plot gives the activation energy required to drive the carrier through the energy barrier. The Arrhenius plots for the Cr- and Co-contacts at different gate voltages are displayed in Fig. 5(a and b). As suggested by the equation, the SBH can be extracted from the slope of the Arrhenius plot. The activation energies at different back-gate voltages are plotted in Fig. 5(c and d) for both Cr- and Co-contacted $MoSe_2$. In these plots, the Schottky barrier height is the activation energy in the flat band condition of the band diagram, seen as the point at which the activation energy ceases to decrease linearly with the gate voltage.[29] This analysis technique has been used to measure the SBH at hundreds of meV (ref. 31 and 38–40) in transition metal dichalcogenide-based devices such as MoS_2, WSe_2, *etc*. Using this same technique, we extracted an SBH of 145 meV for the Cr-contacted $MoSe_2$ FET, whereas we obtained a much smaller SBH of 59 meV for the Co-contact $MoSe_2$ FET. This SBH is very similar to the value measured by Cui *et al.* using Co-contacts[30] on a MoS_2 device through a h-BN tunnel barrier. The SBH could be further reduced using spacer materials like h-BN, which helps modify Co's work function and acts as a tunneling barrier for spin current injection to provide a higher tunneling current from the channel to the drain contact. The ferromagnetic (FM) Co-contacts likely play a significant role in enhancing tunneling and spin-polarized current injection, which may influence the Metal–Insulator Transition (MIT). However, the nature of direct spin current injection from 2D semiconductors to FM contacts is still elusive. Several research groups[29,30] realized the spin current

injection from a 2D semiconductor to the FM metal contact through a thin layer of TiO_2 or h-BN tunnel barrier, which modifies the work function of the FM metal contact on the 2D semiconductor to reduce the SBH. In our device, Co was directly contacted with the $MoSe_2$ layer without any tunnel barrier layer. The FM Co-contact on $MoSe_2$ results in a metal-induced gap state (MIGS) which is influenced not only by the work function of the Cr-contact (non-magnetic contacts), but also by the additional interaction with the magnetic moments at the interface of the ferromagnetic metal and 2D semiconductor. This may influence the change in the electronic structure at the interface, potentially affecting the spin polarization and transport properties of the Co-contact $MoSe_2$ device. In particular, the magnetic interaction of Co-contact can further modify the energy levels of the $MoSe_2$ bandgap, creating unique MIGS characteristics compared to a non-magnetic Cr-contact. This could be the result of such high conductivity in our Co-contact $MoSe_2$ devices compared to the Cr-contact devices. These values indicate that the FM Co-contact is better than the Cr-contact on our $MoSe_2$ devices. Similarly, other magnetic contacts such as Fe and Ni could provide comparable advantages due to their magnetic properties and work function values, which may yield low SBH. All these FM contacts could also be effective for spin current injection when contacted with a suitable tunnel barrier layer between the FM contact and 2D semiconductor. Furthermore, hybridization between the metal and the 2D semiconductor interface may influence charge transfer and tunneling mechanisms. Magnetic metals like Co enhance interface resonances and tune the density of states, leading to improved carrier transport.[41] Furthermore, in contrast, nonmagnetic Cr-contacts experience weaker hybridization and stronger Fermi-level pinning, contributing to the higher SBH.[42] A low SBH value is one of the key parameters for achieving high mobility on the Co-contacted device at low temperatures. A similarly low SBH was also reported using magnetic Permalloy[37,43] and Co-contacted MoS_2 FETs.[31] In addition to the work function of the metal contacts, interface states are more important for tuning the SBH at the 2D semiconductor and metal junction. In contrast to the effect of strong Fermi level pinning using different metal contacts, where the band bending dominates the charge transfer mechanism, the interface resonances can dominate the size of the effective barrier by enhancing the tunneling current through the different metal contacts, particularly when using magnetic contacts.

III. Conclusion

In this report, we have demonstrated how different metal contacts with varying Schottky barrier heights can tune the low-temperature transport properties, showing significant differences in electron density and percolative transport behavior. Magnetic contacts could be best suited for exploring and understanding the intrinsic phase transition of 2D semiconductor-based devices. The observed 2D percolation-driven MIT is consistent throughout the temperature range we studied using Co-contacts, which provided a low Schottky barrier height compared to traditional metal contacts, such as chromium. Although the intrinsic mechanism could be the same in both types of contacts, the ferromagnetic Co-contact tends to inject a higher carrier density than the Cr-contacts. This study will influence the exploration of intrinsic MIT behavior in low dimensional materials, particularly 2D materials, and paves the way for their implementation in novel quantum devices.

Data availability

The raw data for this article including picture and experimental data of current *vs.* gate voltage, conductivity *vs*. temperature and other data presented in the manuscript are available upon request from Dr Nihar R. Pradhan. The data in this manuscript included in the ESI are also available upon request from Dr Nihar R. Pradhan.

Conflicts of interest

There are no conflicts to declare.

Acknowledgements

This work was carried out at Jackson State University, Argonne National Laboratory, IL, USA and the National High Magnetic Field Laboratory, FL, USA. Funding was provided by the U.S. Department of Energy, Office of Science, Office of Basic Energy Sciences program under Award Number DE-SC0024072. Use of the Center for Nanoscale Materials, a Department of Energy Office of Science User Facility, was supported by the U.S. DOE, Office of Basic Energy Sciences, under Contract No. DE-AC02-06CH11357. A portion of this work was performed at the National High Magnetic Field Laboratory, which is supported by the National Science Foundation Cooperative Agreements No. DMR-1644779 and DMR-2128556 and the State of Florida.

References

1 P. Wang, M. Hu, H. Wang, Z. Chen, Y. Feng, J. Wang, W. Ling and Y. Huang, *Adv. Sci.*, 2020, **7**, 2001116.
2 Y. Lee, H. Cho, H. Yoon, H. Kang, H. Yoo, H. Zhou, S. Jeong, G. H. Lee, G. Kim, G. T. Go, J. Seo, T. W. Lee, Y. Hong and Y. Yun, *Adv. Mater. Technol.*, 2023, **8**, 2201067.
3 A. B. Georgescu, P. Ren, A. R. Toland, S. Zhang, K. D. Miller, D. W. Apley, E. A. Olivetti, N. Wagner and J. M. Rondinelli, *Chem. Mater.*, 2021, **33**, 5591–5605.
4 N. Ali, M. Lee, F. Ali, T. D. Ngo, H. Park, H. Shin and W. J. Yoo, *ACS Appl. Mater. Interfaces*, 2023, **15**, 13299–13306.
5 S. Zhang and G. Galli, *npj Comput. Mater.*, 2020, **6**, 170.

6 M. A. Hoque, A. George, V. Ramachandra, E. Najafidehaghani, Z. Gan, R. Mitra, B. Zhao, S. Sahoo, M. Abrahamsson, Q. Liang, J. Wiktor, A. Turchanin, S. Kubatkin, S. Lara-Avila and S. P. Dash, *npj 2D Mater. Appl.*, 2024, **8**, 55.
7 A. Hoffmann, S. Ramanathan, J. Grollier, A. D. Kent, M. J. Rozenberg, I. K. Schuller, O. G. Shpyrko, R. C. Dynes, Y. Fainman, A. Frano, E. E. Fullerton, G. Galli, V. Lomakin, S. P. Ong, A. K. Petford-Long, J. A. Schuller, M. D. Stiles, Y. Takamura and Y. Zhu, *APL Mater.*, 2022, **10**, 070904.
8 Y. J. Lee, Y. Kim, H. Gim, K. Hong and H. W. Jang, *Adv. Mater.*, 2024, **36**, 2305353.
9 H. Li, Q. Li, Y. Li, Z. Yang, R. Quhe, X. Sun, Y. Wang, L. Xu, L. Peng, H. Tian, C. Qiu and J. Lu, *Adv. Funct. Mater.*, 2024, **34**, 2402474.
10 E. Abrahams, P. W. Anderson, D. C. Licciardello and T. V. Ramakrishnan, *Phys. Rev. Lett.*, 1979, **42**, 673–676.
11 S. Ahn and S. Das Sarma, *Phys. Rev. B*, 2022, **105**, 115114.
12 C. Zhang, S. Kc, Y. Nie, C. Liang, W. G. Vandenberghe, R. C. Longo, Y. Zheng, F. Kong, S. Hong, R. M. Wallace and K. Cho, *ACS Nano*, 2016, **10**, 7370–7375.
13 B. H. Moon, *Emergent Mater.*, 2021, **4**, 989–998.
14 Z. Zhao, H. Zhang, H. Yuan, S. Wang, Y. Lin, Q. Zeng, G. Xu, Z. Liu, G. K. Solanki, K. D. Patel, Y. Cui, H. Y. Hwang and W. L. Mao, *Nat. Commun.*, 2015, **6**, 7312.
15 N. R. Pradhan, C. Garcia, B. Chakrabarti, D. Rosenmann, R. Divan, A. V. Sumant, S. Miller, D. Hilton, D. Karaiskaj and S. A. McGill, *Nanoscale*, 2023, **15**, 2667–2673.
16 Y. Liu, N. O. Weiss, X. Duan, H.-C. Cheng, Y. Huang and X. Duan, van der Waals heterostructures and devices, *Nat. Rev. Mater.*, 2016, **1**, 16042.
17 R. K. Ghosh and S. Datta, in *2016 International Conference on Simulation of Semiconductor Processes and Devices (SISPAD)*, 2016, pp. 93–96.
18 D. Zhou, Y. Zhou, C. Pu, X. Chen, P. Lu, X. Wang, C. An, Y. Zhou, F. Miao, C. H. Ho, J. Sun, Z. Yang and D. Xing, *npj Quantum Mater.*, 2017, **2**, 19.
19 N. R. Pradhan, D. Rhodes, Y. Xin, S. Memaran, L. Bhaskaran, M. Siddiq, S. Hill, P. M. Ajayan and L. Balicas, *ACS Nano*, 2014, **8**, 7923–7929.
20 D. Zhang, C. Wen, J. B. Mcclimon, P. Masih Das, Q. Zhang, G. A. Leone, S. V. Mandyam, M. Drndić, A. T. C. Johnson Jr. and M.-Q. Zhao, *Adv. Electron. Mater.*, 2021, **7**, 2001219.
21 B. Radisavljevic and A. Kis, *Nat. Mater.*, 2013, **12**, 815–820.
22 S. Das Sarma, M. P. Lilly, E. H. Hwang, L. N. Pfeiffer, K. W. West and J. L. Reno, *Phys. Rev. Lett.*, 2005, **94**, 136401.
23 S. K. Mallik, R. Padhan, M. C. Sahu, S. Roy, G. K. Pradhan, P. K. Sahoo, S. P. Dash and S. Sahoo, *ACS Appl. Mater. Interfaces*, 2023, **15**, 36527–36538.
24 V. Podzorov, M. E. Gershenson, C. Kloc, R. Zeis and E. Bucher, *Appl. Phys. Lett.*, 2004, **84**, 3301–3303.
25 N. R. Pradhan, D. Rhodes, Q. Zhang, S. Talapatra, M. Terrones, P. M. Ajayan and L. Balicas, *Appl. Phys. Lett.*, 2013, **102**, 123105.
26 N. R. Pradhan, Z. Lu, D. Rhodes, D. Smirnov, E. Manousakis and L. Balicas, *Adv. Electron. Mater.*, 2015, **1**, 1500215.
27 S. K. Mallik, R. Padhan, S. Roy, M. C. Sahu, S. Sahoo and S. Sahoo, *ACS Appl. Nano Mater.*, 2024, **7**, 4796–4804.
28 S. Fathipour, N. Ma, W. S. Hwang, V. Protasenko, S. Vishwanath, H. G. Xing, H. Xu, D. Jena, J. Appenzeller and A. Seabaugh, *Appl. Phys. Lett.*, 2014, **105**, 192101.
29 A. Allain, J. Kang, K. Banerjee and A. Kis, *Nat. Mater.*, 2015, **14**, 1195–1205.
30 X. Cui, E. M. Shih, L. A. Jauregui, S. H. Chae, Y. D. Kim, B. Li, D. Seo, K. Pistunova, J. Yin, J. H. Park, H. J. Choi, Y. H. Lee, K. Watanabe, T. Taniguchi, P. Kim, C. R. Dean and J. C. Hone, *Nano Lett.*, 2017, **17**, 4781–4786.
31 A. Dankert, L. Langouche, M. V. Kamalakar and S. P. Dash, *ACS Nano*, 2014, **8**, 476–482.
32 Y. Liu, W. Wu and W. A. Goddard, *J. Am. Chem. Soc.*, 2018, **140**, 550.
33 X. Li, J. T. Mullen, Z. Jin, K. M. Borysenko, M. Buongiorno Nardelli and K. W. Kim, *Phys. Rev. B: Condens. Matter Mater. Phys.*, 2013, **87**, 115418.
34 N. R. Pradhan, A. McCreary, D. Rhodes, Z. Lu, S. Feng, E. Manousakis, D. Smirnov, R. Namburu, M. Dubey, A. R. Hight Walker, H. Terrones, M. Terrones, V. Dobrosavljevic and L. Balicas, *Nano Lett.*, 2015, **15**, 8377–8384.
35 L. A. Tracy, E. H. Hwang, K. Eng, G. A. Ten Eyck, E. P. Nordberg, K. Childs, M. S. Carroll, M. P. Lilly and S. Das Sarma, *Phys. Rev. B: Condens. Matter Mater. Phys.*, 2009, **79**, 235307.
36 M. Imada, A. Fujimori and Y. Tokura, *Rev. Mod. Phys.*, 1998, **70**, 1039.
37 S. Gupta, F. Rortais, R. Ohshima, Y. Ando, T. Endo, Y. Miyata and M. Shiraishi, *Sci. Rep.*, 2019, **9**, 17032.
38 N. Kaushik, A. Nipane, F. Basheer, S. Dubey, S. Grover, M. M. Deshmukh and S. Lodha, *Appl. Phys. Lett.*, 2014, **105**, 113505.
39 S. Lee, A. Tang, S. Aloni and H. S. Philip Wong, *Nano Lett.*, 2016, **16**, 276–281.
40 S. Das, H.-Y. Chen, A. V. Penumatcha and J. Appenzeller, *Nano Lett.*, 2013, **13**, 100–105.
41 K. F. Mak, J. Shan and D. C. Ralph, *Nat. Rev. Phys.*, 2019, **1**(11), 646–661.
42 J. Meng, C. Lee and Z. Li, *Sci. Bull.*, 2024, **69**(9), 1342–1352.
43 W. Wang, Y. Liu, L. Tang, Y. Jin, T. Zhao and F. Xiu, *Sci. Rep.*, 2014, **4**, 6928.